(Zr) and niobium (Nb) were completely removed from the surface layer to a depth of 250 nm and that Ca and oxygen (O_2) penetrated into the surface layer to depths of 500 nm and 1500 nm, respectively. Both of them showed a gradual decrease with increasing depth. Note that the Ca content is slightly decreased at the top surface.

Figure 2 shows FE-SEM photographs of the surfaces of the Ti–15Zr–4Nb–4Ta alloy subjected to the NaOH, $CaCl_2$, heat, and water treatments compared with the untreated alloy. A fine network structure was formed on the nanometer scale by the first NaOH treatment; it was essentially unchanged by the subsequent $CaCl_2$ and heat treatments, but slightly modified with small particles after the final water treatment.

Cross-sectional FE-SEM photographs of these alloy samples are shown in Fig. 3. It can be seen that the fine network structure formed by the first NaOH treatment consists of featherlike phases about 500 nm in length, elongated perpendicular to the surface. The density of the surface layer increased with increasing depth. Its structure was essentially unchanged by the subsequent $CaCl_2$, heat, and water treatments.

Figure 4 shows TF-XRD and FT-Raman profiles of the surface of the untreated alloy samples and those subjected to the NaOH, $CaCl_2$, heat, and water treatments. Broad, small peaks attributed to sodium hydrogen titanate, $Na_xH_{2-x}Ti_3O_7$ [18, 19], appeared after the first NaOH treatment. They were almost unchanged even after the second $CaCl_2$ treatment, indicating that the sodium hydrogen titanate on the surface was isomorphously transformed into calcium hydrogen titanate, $Ca_xH_{2-2x}Ti_3O_7$, by substituting Na in the sodium hydrogen titanate with Ca. The calcium hydrogen titanate was dehydrated to transform into calcium titanate whose phases were assumed to be $CaTi_4O_9$ and $CaTi_2O_4$ [20, 21], and rutile by the subsequent heat treatment. Thus, the formed calcium titanate remained even after the final water treatment, accompanied by small amounts of newly formed anatase. All of these phases are considered to occur at nanometer sizes from their broad X-ray diffraction peaks.

The scratch resistance of the surface of the Ti–15Zr–4Nb–4Ta alloy was as low as 10 mN after the first NaOH and second $CaCl_2$ treatments. This remarkably increased up to about 170 mN after the heat treatment and did not decrease even after the final water treatment.

3.2 Apatite formation

Figure 5 shows FE-SEM photographs of the surfaces of the alloy samples that were soaked in SBF for 3 d after the NaOH, $CaCl_2$, heat, and water treatments. The figure shows that some spherical precipitates were formed on the NaOH-treated alloy. These spherical precipitates increased slightly after the second $CaCl_2$ treatment, but were lost with the heat treatment. After the final water treatment, they remarkably increased to cover the whole surface within 3 d in SBF. These spherical precipitates were identified as crystalline

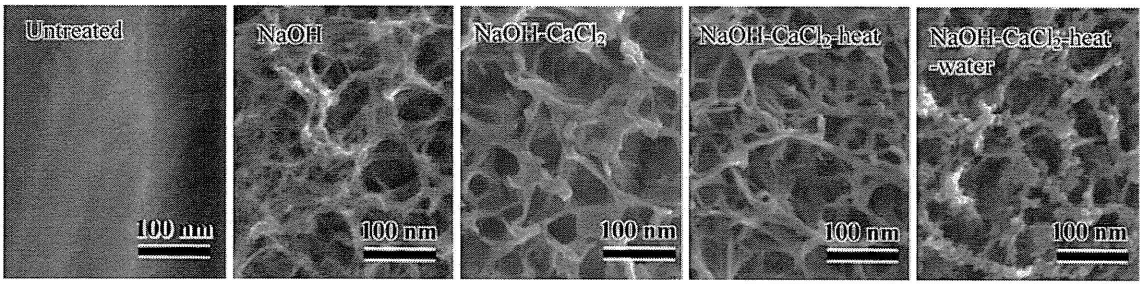

Fig. 2 FE-SEM photographs of the surfaces of Ti–15Zr–4Nb–4Ta alloy after NaOH, $CaCl_2$, heat and water treatments in comparison with that of untreated alloy

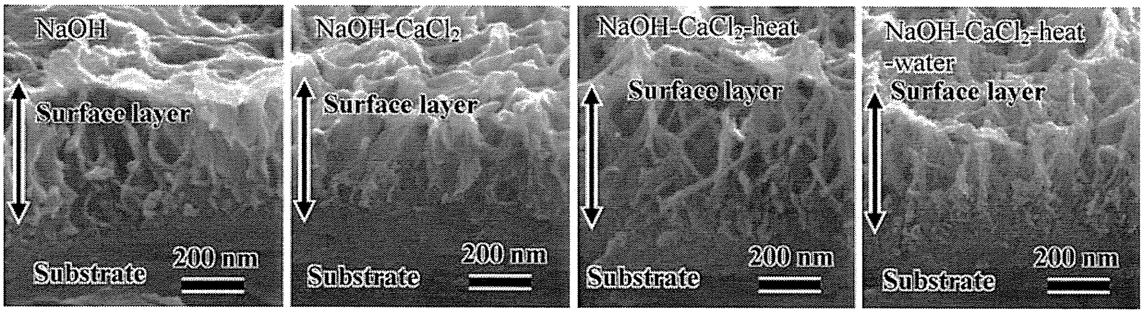

Fig. 3 FE-SEM photographs of the cross-sections of Ti–15Zr–4Nb–4Ta alloy after NaOH, $CaCl_2$, heat and water treatments

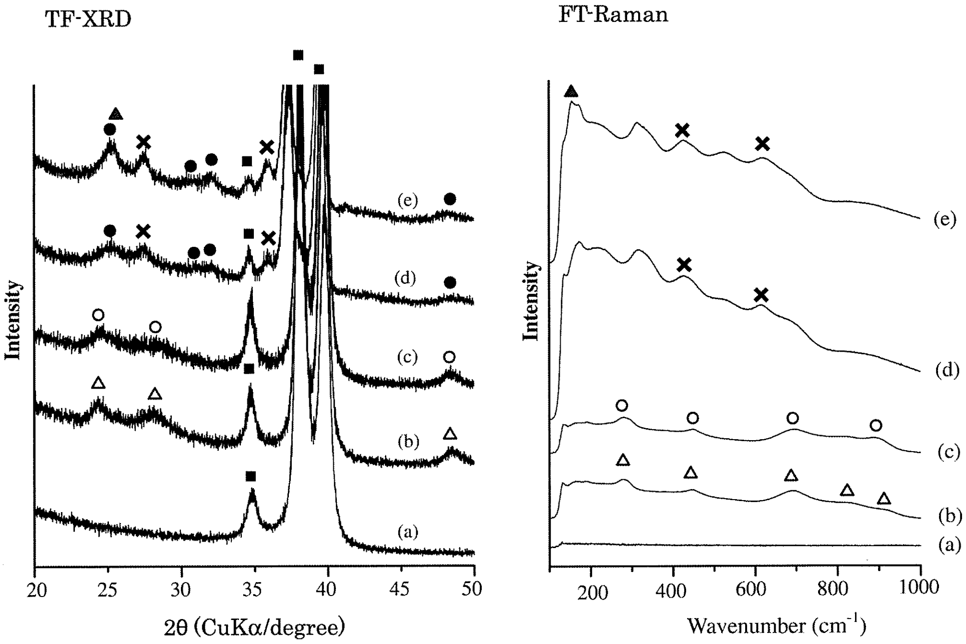

Fig. 4 TF-XRD and FT-Raman profiles of the surfaces of Ti–15Zr–4Ta–4Nb alloy (a) before and after (b) NaOH treatment, (c) NaOH and $CaCl_2$ treatments, (d) NaOH, $CaCl_2$ and heat treatments and (e) NaOH, $CaCl_2$, heat and water treatments. (■) α-Titanium; (△) Sodium hydrogen titanate ($Na_xH_{2-x}Ti_3O_7$); (○) Calcium hydrogen titanate ($Ca_xH_{2-2x}Ti_3O_7$); (●) Calcium titanate ($CaTi_4O_9$, $CaTi_4O_9$); (×) Rutile; (▲) Anatase

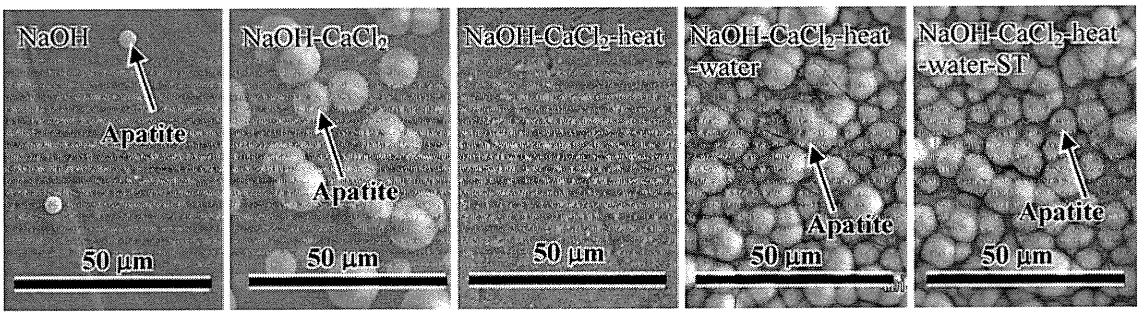

Fig. 5 FE-SEM photographs of the surfaces of Ti–15Zr–4Ta–4Nb alloy that were soaked in SBF for 3 days after NaOH, $CaCl_2$, heat and water treatments, and after subsequent stability test (ST) in humid environment

apatite by TF-XRD. The high apatite-forming ability was maintained even after the stability test in a humid environment.

4 Discussion

Structural changes of the surface of the Ti–15Zr–4Nb–4Ta alloy because of the NaOH, $CaCl_2$, heat, and water treatments are schematically shown in Fig. 6, based on the experimental results. A brush-like structure about 500 nm in thickness, consisting of featherlike phases elongated perpendicular to the surface, was formed on the surface of the alloy by the NaOH treatment. The featherlike phases consisted of nanosized sodium hydrogen titanate that takes a layered structure [19] and, hence, easily substitutes Ca^{2+} ions for Na^+ ions to form a calcium hydrogen titanate, by the $CaCl_2$ treatment. Thus, the formed calcium hydrogen titanate transformed into calcium titanates such as $CaTi_4O_9$ and $CaTi_2O_4$, and rutile by dehydration on the subsequent heat treatment. The calcium titanates and rutile were mostly unchanged by the water treatment, but a small amount of them transformed into anatase by releasing Ca^{2+} ions. From the experimental results described above, it is apparent that the apatite-forming ability of the Ti–15Zr–4Nb–4Ta alloy is slightly induced in the body environment by the NaOH and $CaCl_2$ treatments. However, the treated alloy has a poor scratch resistance and, hence, is unsuitable for practical applications. It was given high scratch resistance by the subsequent heat treatment but lost its apatite-forming ability. It developed a high scratch resistance and high apatite-forming ability as well as stability in a humid environment after the final water treatment. These variations of the apatite-forming ability of the alloy with the chemical and heat treatments are interpreted in terms of surface structural changes as follows.

Induction of the apatite-forming ability of the alloy by the first NaOH treatment is attributed to the formation

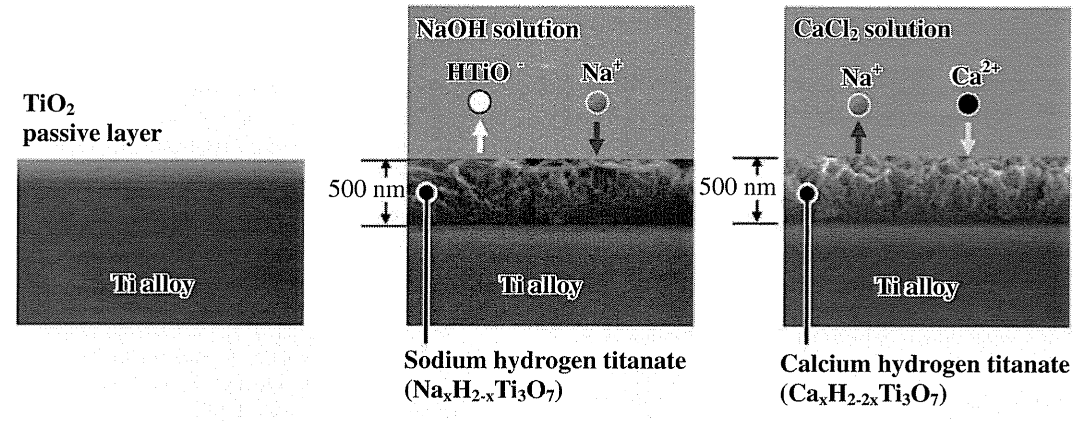

(a) Before treatment

(b) After NaOH treatment

(c) After NaOH and $CaCl_2$ treatments

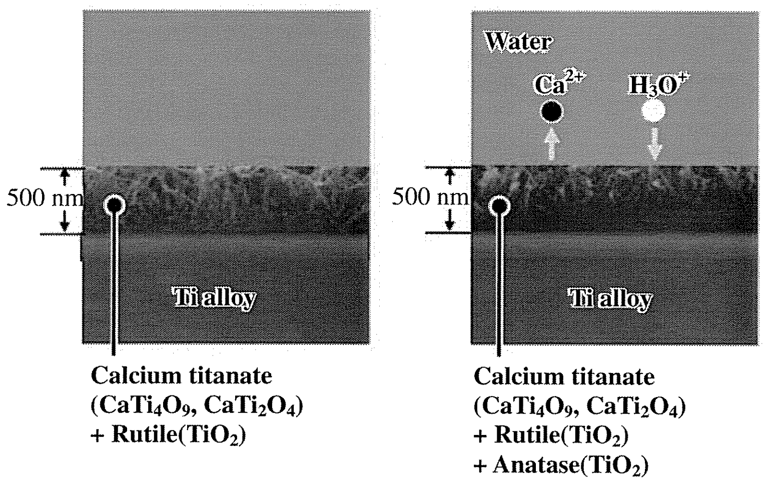

(d) After NaOH, $CaCl_2$ and heat treatments

(e) After NaOH, $CaCl_2$, heat and water treatments

Fig. 6 Schematic illustration of structural changes on the surface of Ti–15Zr–4Nb–4Ta alloy (**a**) by NaOH (**b**), $CaCl_2$ (**c**), heat (**d**) and water (**e**) treatments

of sodium hydrogen titanate on its surface. In SBF, the sodium hydrogen titanate releases its Na^+ ions via exchange with H_3O^+ ions to form Ti–OH groups on its surface. Thus, the formed Ti–OH groups induce apatite formation as earlier described for the NaOH- and heat-treated Ti metal [22–24]. The increased apatite-forming ability of the alloy due to the $CaCl_2$ treatment is attributed to the formation of calcium hydrogen titanate on its surface. The calcium hydrogen titanate more effectively induces apatite formation because the released Ca^{2+} ions increase the ionic activity product of the apatite in the surrounding SBF more effectively than the Na^+ ions do. The loss of the apatite-forming ability of the alloy due to the heat treatment is attributed to the reduced mobility of the Ca^{2+} ions in calcium titanate. The remarkable increase of the apatite-forming ability of the alloy due to the subsequent water treatment is a result of the increased mobility of the Ca^{2+} ions in the calcium titanate by incorporation of H_3O^+ ions during the water treatment. The incorporation of H_3O^+ ions at the surface of the alloy subjected to the water treatment is proved by the decrease in Ca content at its top surface, observed by AES in Fig. 1. The mobility of the Ca^{2+} ions in the calcium titanate is, however, not so high that the Ca content is appreciably decreased in a humid environment. As a result, the high apatite-forming ability of the alloy can be maintained even in 95% relative humidity at 80°C for at least 1 week.

Generally, the mechanical properties of Ti-based alloys are liable to be changed by heat treatment. It is reported, however, that the tensile strength, proof strength, and ductility (reduction in area and elongation) of Ti–15Zr–4Nb–4Ta alloys are hardly affected by heat treatment below 775°C for 1 h [6]. Therefore, heat treatment at 600°C after the NaOH and $CaCl_2$ treatments, which was used in the present study, does not have an adverse affect on the mechanical strength of the present alloy.

Thus, the treated alloy is expected to form bone-like apatite on its surface, even in the living body, and bond to living bone.

5 Conclusion

Ti–15Zr–4Nb–4Ta alloy, which is free from cytotoxic elements and shows high mechanical strength, can be given a high apatite-forming ability, which is maintained even in a humid environment, and scratch resistance by NaOH, $CaCl_2$, heat, and water treatments. It is believed that this bioactive alloy will be useful in implants in the orthopedic and dental fields in the next generation.

Acknowledgements This work was supported by Translational Research Promotion Project in Health Assurance Program entrusted from the New Energy and Indusrial Techology Development Organization (NEDO). We thank Dr. Yoshimitsu Okazaki for the supply of the alloy.

References

1. Waters MD, Gardner DE, Coffin DL. Cytotoxic effects of vanadium on rabbit alveolar macrophages in vitro. Toxicol Appl Pharmacol. 1974;28:253–63.
2. Steinemann SG. In: Winter GD, Leray JL, de Goot K, editors. Evaluation of biomaterials. New York: Wiley; 1980. p. 1–34.
3. Kawahara H, Ochi S, Tanetani K, Kato K, Isogai M, Mizuno H, et al. Biological testing of dental materials. J Jpn Soc Dent Apparatus Mater. 1963;4:65–75.
4. Maehara K, Doi K, Matsushita T, Sasaki Y. Application of vanadium-free titanium alloys to artificial hip joints. Mater Trans. 2002;43:2936–42.
5. Okazaki Y, Rao S, Ito Y, Tateishi T. Corrosion resistance, mechanical properties, corrosion fatigue strength and cytocompatibility of new Ti alloys without Al and V. Biomaterials. 1998; 19:1197–215.
6. Japanese Industrial Standards. JIST7401-4: titanium materials for surgical implant applications. Part 4. Wrought titanium 15-zirconium 4-niobium 4-tantalum alloy. Tokyo: JISC; 2002.
7. American Society for Testing and Materials. ASTM STP 1272: mechanical and tribological properties and biocompatibility of diffusion hardened Ti–13Nb–13Zr—a new titanium alloy for surgical implants, medical applications of titanium and its alloys: the material and biological issues. Philadelphia: ASTM; 1996.
8. American Society for Testing and Materials. ASTM STP 1272: characterization of Ti–15Mo Beta titanium alloy for orthopedic implant applications, medical applications of titanium and its alloys: the materials and biological issues. Philadelphia: ASTM; 1996.
9. American Society for Testing and Materials. ASTM STP 1471: super elastic functional β titanium alloy with low Young's modulus for biomedical applications. Philadelphia: ASTM; 2006.
10. Kokubo T, Miyaji F, Min-Kim H, Nakamura T. Spontaneous formation of bone-like apatite layer on chemically treated titanium metal. J Amer Ceram Soc. 1996;79:1127–9.
11. Yan QW, Nakamura T, Kobayashi M, Kokubo T, Kim HM, Miyaji F. Bone-bonding behavior of titanium implants prepared via chemical treatment. In: Kokubo T, Nakamura T, Miyaji F, editors. Bioceramics, vol. 9. London: Elsevier; 1996. p. 305–8.
12. Yan QW, Nakamura T, Kobayashi M, Kim HM, Kokubo T. Bonding of chemically treated titanium implants to bone. J Biomed Mater Res. 1997;37:267–75.
13. Kim HM, Miyaji F, Kokubo T, Nakamura T. Preparation of bioactive Ti and its alloy via simple chemical surface treatment. J Biomed Mater Res. 1996;32:409–17.
14. Kim HM, Takadama H, Kokubo T, Nishiguchi S, Nakamura T. Formation of a bioactive graded surface structure on Ti–15Mo–5Zr–3Al alloy by chemical treatment. Biomaterials. 2000;21: 353–8.
15. Nishiguchi S, Kato H, Fujita H, Kim HM, Miyaji F, Kokubo T, et al. Enhancement of bone-bonding strength of titanium alloy implants by alkali and heat treatments. J Biomed Mater Res. 1999;48:689–96.
16. Kokubo T, Takadama H. How useful is SBF in predicting in vivo bone bioactivity? Biomaterials. 2006;27:2907–15.
17. International Organization for Standardization. ISO 23317:2007: implants for surgery—in vitro evaluation for apatite-forming ability of implant materials. Switzerland: ISO; 2007.
18. Sun X, Li Y. Synthesis and characterization of ion-exchangeable titanate nanotubes. Chem Eur J. 2003;9:2229–38.
19. Morgado E Jr, de Abreu MAS, Pravia ORC, Marinkovic BA, Jardim PM, Rizzo FC, et al. A study on the structure and thermal stability of titanate nanotubes as a function of sodium content. Sol St Sci. 2006;8:888–900.
20. Joint Committee on Powder Diffraction Standards (JCPDS) Powder Diffraction Data File 00-026-0333.
21. Joint Committee on Powder Diffraction Standards (JCPDS) Powder Diffraction Data File 01-072-1134.
22. Takadama H, Kim HM, Kokubo T, Nakamura T. An X-ray photoelectron spectroscopy study of the process of apatite formation on bioactive titanium metal. J Biomed Mater Res. 2001;55: 185–93.
23. Takadama H, Kim HM, Kokubo T, Nakamura T. TEM-EDX study of the mechanism of bonelike apatite formation on bioactive titanium metal in simulated body fluid. J Biomed Mater Res. 2001;57:441–8.
24. Kim HM, Himeno T, Kawashita M, Lee JH, Kokubo T, Nakamura T. Surface potential change in bioactive titanium metal during the process of apatite formation in simulated body fluid. J Biomed Mater Res. 2003;67:1305–9.

Journal of the Ceramic Society of Japan 118 [1] 19-24 2010 **Paper**

Apatite formation on surface titanate layer with different Na content on Ti metal

Takahiro KAWAI,[†] Takashi KIZUKI,[*] Hiroaki TAKADAMA,[*] Tomiharu MATSUSHITA,[*]
Hidero UNUMA, Takashi NAKAMURA[**] and Tadashi KOKUBO[*]

Department of Chemistry and Chemical Engineering, Graduate School of Science and Engineering, Yamagata University,
4–3–16, Jonan, Yonezawa, Yamagata 992–8510
[*]Department of Biomedical Science, College of Life and Health Sciences, Chubu University,
1200, Matsumoto-cho Kasugai, Aichi 487–8501
[**]Department of Orthopaedic Surgery, Graduate School of Medical, Kyoto University,
54, Kawahara-cho, Shogoin, Sakyo-ku, Kyoto 606–8507

It was early shown that Ti metal spontaneously bonds to living bone through an apatite layer formed on its surface in the living body, when it was subjected to NaOH and heat treatment to form a sodium titanate on its surface. This kind of bioactive Ti metal was applied to artificial hip joint and already clinically used in Japan. During the study of fabrication process of the hip joint, it was found that sodium content of the surface layer of the Ti metal is largely varied with washing condition after the NaOH treatment, and that apatite-forming ability of the NaOH- and heat-treated Ti metal is liable to decrease in humid environment for a long period. In the present study, the sodium content of the surface layer of the Ti metal was systematically changed by water or HCl treatment after NaOH treatment. Effect of the sodium content of the surface layer on apatite-forming ability in a simulated body fluid and its stability in humid environment of the NaOH- and heat-treated Ti metal were investigated. As a result, it was found that the NaOH- and heat-treated Ti metal gives high and stable apatite-forming ability, when the Ti metal was treated with water after the NaOH treatment to remove partially sodium ions in the surface layer, and subjected to heat treatment.

Key-words : Titanium, Surface ceramic layer, Sodium content, Apatite-forming ability, Scratch resistance

[Received July 21, 2009; Accepted November 19, 2009]

1. Introduction

It has been shown that Ti metal and its alloys with a sodium titanate layer on their surfaces by NaOH and heat treatments induces the formation of a bone-like apatite layer on the surface in the living body; this apatite layer allows the Ti metal to bond to living bone.[1)] These treatments were applied to a porous Ti metal layer on artificial hip joint of Ti–6Al–2Nb–Ta alloy. This bioactive hip joint has been clinically used in Japan since October 2007.

While the fabrication process for a reliable artificial hip joint was being established, it was found that the sodium content of the surface layer of the Ti metal is largely varied with washing condition after the NaOH treatment.

In the present study, the sodium content of the surface layer was systematically changed by exposing the NaOH-treated Ti metal to water or HCl solution under the given conditions after the NaOH treatment. The Ti metals formed with the surface layers of different sodium contents were heat-treated and their apatite-forming abilities in a simulated body fluid (SBF) were investigated as indications of their bone-bonding ability.

Effect of the sodium content on apatite-forming ability of the NaOH-treated Ti metal has been studied by Jonášová et al.[2)] for the Ti metals not subjected to heat treatment. These Ti metals give only low scratch resistance and are difficult to be used clinically. In the present studies, similar studies were performed for Ti metals heat-treated after the NaOH treatment, which have enough scratch resistance for clinical applications, in comparison with the results of Ti metals before heat treatment.

During the studies of fabrication process of the hip joint, it was also found that the apatite-forming ability of the NaOH- and heat-treated Ti metal is liable to decrease in humid environment after a long period. In the present study, stability of the apatite-forming ability of the NaOH- and heat-treated Ti metal in humid environment was also investigated in terms of the sodium content in its surface layer.

2. Experimental procedure

2.1 Preparation of surface layers of different Na contents on Ti plates

Pure Ti plates (purity: 99.9%, The Nilaco Corp.) were cut into squares (10 mm × 10 mm × 1 mm), abraded with a #400 diamond plate, washed in acetone, 2-propanol and ultrapure water in this order for 30 min, respectively, and dried at 40°C. The plates were immersed in 5 mL of 5-M NaOH at 60°C for 24 h under shaking at 120 strokes·min^{-1} on a bath shaker (Personal H–10, Taitec Co., Ltd.). After being taken out from the solution, the Ti plates were gently washed with ultrapure water for 30 s and dried at 40°C for 24 h. They were heated in an electric furnace (FT–1200G–300, Full-Tech Corp.) at a rate of 5°C·min^{-1} and kept at 600°C for 1 h, followed by natural cooling in the furnace. Some of the NaOH-treated specimens were immersed in 10 mL or 200 mL of ultrapure water or 10 mL of 0.5-mM HCl for given

---

[†] Corresponding author: T. Kawai; E-mail: t-kawai@yz.yamagata-u.ac.jp

Table 1. Examined Samples and Their Treatments

Samples	NaOH-treatment (5 M–NaOH at 60°C for 24 h)	Water-treatment (H_2O at 40°C for 3–24 h)	HCl-treatment (0.5 mM–HCl at 40°C for 24 h)	Heat-treatment (600°C for 1 h)
A	+	–	–	–
A-W(3 h)	+	+ (10 mL, 3 h)	–	–
A-W(6 h)	+	+ (10 mL, 6 h)	–	–
A-W(24 h)	+	+ (10 mL, 24 h)	–	–
A-20W(24 h)	+	+ (200 mL, 24 h)	–	–
A-0.5HC(24 h)	+	–	+	–
A-H	+	–	–	+
A-W(3 h)-H	+	+ (10 mL, 3 h)	–	+
A-W(6 h)-H	+	+ (10 mL, 6 h)	–	+
A W(24 h)-H	+	+ (10 mL, 24 h)	–	+
A-20W(24 h)	+	+ (200 mL, 24 h)	–	+
A-0.5HC(24 h)-H	+	–	+	+

+; Treated.
–; Not treated.

periods, and washed and dried before the heat treatment in order to remove the given amounts of Na ions. Then they were heat-treated by the same method as described above. The examined specimens and their treatments are summarized in **Table 1.**

2.2 Structural analysis of the surface layers on the Ti plates

The atomic percentages of Na in the surface layers of the Ti plates were measured by energy dispersive X-ray (EDX, EMAX-7000, Horiba, Ltd.) analysis, where the acceleration voltage was 9 kV, the detection area was 43 μm × 32 μm, and the working distance was 15 mm. The surface morphologies were observed under a field emission scanning electron microscope (FE–SEM, S–4300, Hitachi, Ltd.), where the acceleration voltage was 15 kV. The constituent phases were verified by thin-film X-ray diffraction (TF–XRD, RINT–2000, Rigaku Co.). The measurement was performed using a Cu Kα X-ray source at 40 kV and 40 mA, and the glancing angle of the incident beam was set at 1° against the sample surfaces. The structure of the surface layers was also examined by Fourier transform confocal laser Raman spectroscopy (FT-Raman, LabRAM300, Horiba Jobin Yvon, France) with an Ar laser (wavelength: 514 nm).

2.3 Measurement of the scratch resistance of the surface layers of the Ti plates

The scratch resistance of the surface layers was measured using a thin-film scratch tester (CSR–2000, Rhesca Co., Ltd.) equipped with a stylus 5 μm in diameter (spring constant: 200 g·mm^{-1}). In this measurement, the amplitude was 100 μm, the scratch speed was 10 μm·s^{-1}, and the load rate was 100 mN·min^{-1} (based on Japan Industrial Standard R–3255).

2.4 Evaluation of the apatite-forming ability of the surface layers of the Ti plates

The specimens listed in Table 1 were soaked in simulated body fluids (SBFs) with ion concentrations nearly equal to those of human blood plasma at 36.5°C for 1 d. The SBFs were prepared according to the recipes previously reported.[3),4)] Their apatite-forming abilities were evaluated by observing area ratio of surfaces which were covered with apatite under FE–SEM.

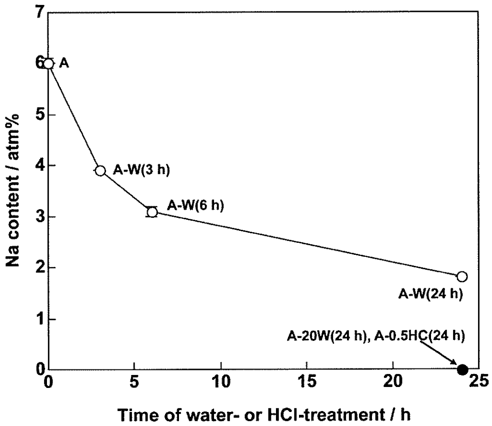

Fig. 1. Atomic percentages of sodium in the surface layers of Ti metal subjected to NaOH, and water or HCl treatments (Measurement was performed at three independent areas).

In order to examine stabilities of the apatite-forming abilities of the surface layers, some specimens shown in Table 1 were kept in 95% relative humidity at 80°C for 1 w. Their apatite-forming abilities were evaluated by the same method and compared with those of the specimens not kept in the humid environment.

3. Results

3.1 Structure of the surface layers formed on the Ti plates

Figure 1 shows the changes in the atomic percentages of Na in the surface layers of the Ti plates subjected to water treatment or HCl treatment after the NaOH treatment. Sodium at 6.0 atm% was detected on the Ti plates treated with NaOH solution only (Sample A). This value decreased with soaking in 10 mL of water, and reached 1.9 atm% after 24 h. When the same plates were soaked in 200 mL of water or 10 mL of 0.5-mM HCl for 24 h, the Na content decreased to levels below the limit of measurement. These Na contents were not changed by the subsequent heat treatment.

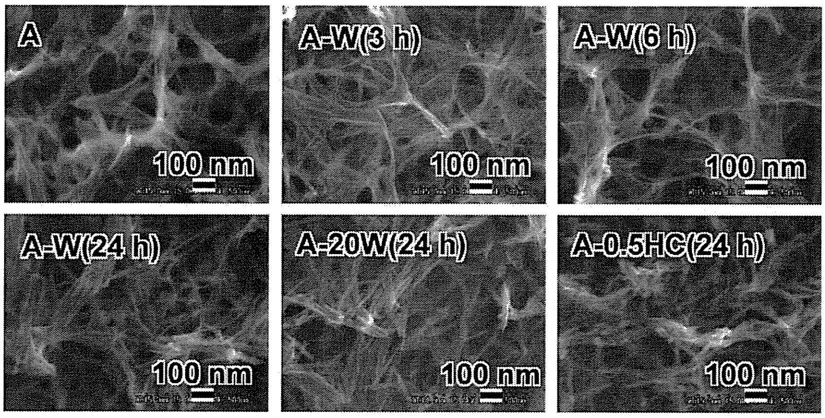

Fig. 2. FE–SEM images of the surfaces of Ti plates subjected to NaOH, and water or HCl treatments.

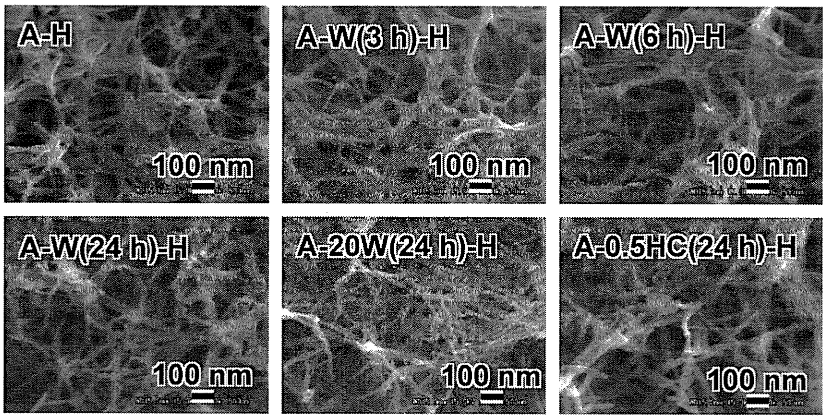

Fig. 3. FE–SEM images of the surfaces of Ti plates subjected to heat-treatments after the NaOH, and water or HCl treatments.

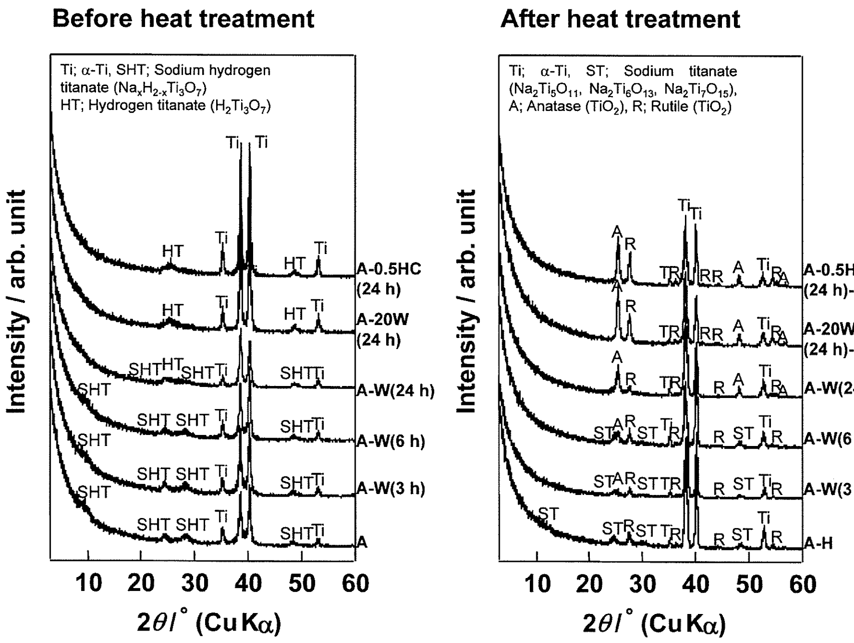

Fig. 4. TF–XRD patterns of the surfaces of Ti plates subjected to NaOH, and water or HCl treatments, which were examined before and after the subsequent heat treatments. (Ti; α-Ti, SHT; Sodium hydrogen titanate ($Na_xH_{2-x}Ti_3O_7$), HT; Hydrogen titanate ($H_2Ti_3O_7$), ST; Sodium titanate ($Na_2Ti_5O_{11}$, $Na_2Ti_6O_{13}$, $Na_2Ti_7O_{15}$), A; Anatase (TiO_2), R; Rutile (TiO_2)).

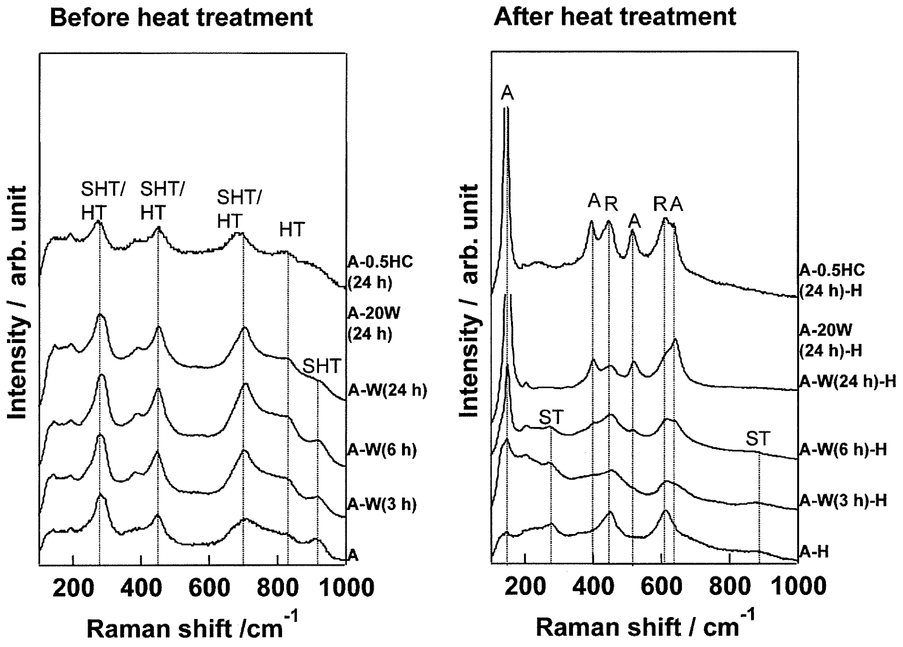

Fig. 5. Raman spectra of the surfaces of Ti plates subjected to NaOH, and water or HCl treatments, which were measured before and after the subsequent heat treatments. (SHT; Sodium hydrogen titanate, HT; Hydrogen titanate, A; Anatase, R; Rutile, ST; Sodium titanate).

Figure 2 shows FE–SEM images of the surfaces of NaOH-treated Ti plates subjected to water or HCl treatment without heating. A fine network structure was formed as a result of the NaOH treatment, and it remained essentially unchanged in spite of subsequent water or HCl treatment.

Figure 3 shows FE–SEM images of the surfaces of NaOH-treated Ti plates subjected to heat treatment after the water or HCl treatment. It can be seen from the figure that the fine network structure observed in all the examined specimens before the heat treatment remained essentially unchanged even after the heat treatment.

Figure 4 shows TF–XRD patterns of the surfaces of Ti plates subjected to water or HCl treatments after the soaking in the NaOH solution, before and after the subsequent heat treatment. Ti metal subjected to NaOH treatment only (Sample A) gave small and broad diffraction peaks ascribed to sodium hydrogen titanates ($Na_xH_{2-x}Ti_yO_{2y+1}$; $0 < x < 2$ and $y = 2$, 3 or 4) or their hydrated analogues ($Na_xH_{2-x}Ti_yO_{2y+1}\cdot nH_2O$),[5)–10)] besides the peaks of Ti metal. Small new peaks ascribed to hydrogen titanates ($H_2Ti_yO_{2y+1}$; $y = 2$, 3 or 4)[9)–12)] appeared after the subsequent 24 h water treatment, and the former peaks disappeared after a water treatment in a larger volume or an HCl treatment.

When they were heat-treated, the Ti plates subjected only to NaOH treatment (Sample A–H) gave small and broad peaks ascribed to sodium titanates ($Na_2Ti_yO_{2y+1}$; $y = 5$, 6, etc.)[9),12),13)] and rutile (TiO_2). The sodium titanate peaks were weakened, and peaks ascribed to anatase (TiO_2) newly appeared with increasing water treatment time after the NaOH treatment; the new anatase peaks completely replaced the sodium titanate peaks after 24 h of water treatment. The anatase and rutile peaks grew as the water volume increased, as well as with HCl treatment.

Figure 5 shows FT-Raman spectra of the surfaces of NaOH-treated Ti plates subjected to water or HCl treatment, before and after the subsequent heat treatment. The Ti metal treated only with the NaOH solution gave only peaks ascribed to sodium hydrogen titanates (SHT in the figure). When the NaOH-treated Ti metal was soaked in water, peaks ascribed to hydrogen titanates (HT in the figure) were newly observed. The peaks of the sodium hydrogen titanates disappeared when the NaOH-treated Ti metal was soaked in a larger volume of water or in HCl solution for 24 h. After the above-mentioned metal samples were heat-treated, they gave peaks ascribed to sodium titanates and rutile. The sodium titanate peaks decreased and the peaks ascribed to anatase increased with increasing water treatment time after the NaOH treatment. These results are consistent with

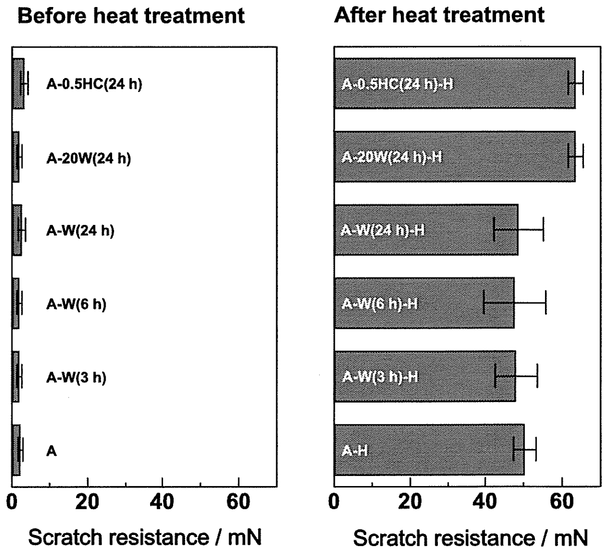

Fig. 6. Scratch resistance of surface layers on Ti plates subjected to NaOH, and water or HCl treatments, which were measured before and after the subsequent heat treatments (Measurements were performed at three different areas).

the results of the TF–XRD analysis.

3.2 Scratch resistance of the surface layers of the Ti plates

Figure 6 shows scratch resistance of the surface layers on NaOH-treated Ti plates with water or HCl treatment, measured before and after the subsequent heat treatment. It can be seen from the figure that the surface layers without the heat treatment showed only a low scratch resistance, but imparted a remarkably higher resistance after the heat treatment. Especially the surface layers subjected to water treatment in a larger volume or HCl treatment showed higher scratch resistance. That is to say, the heat treatment is essential to enhance the scratch resistance of the surface layer regardless of the sodium content.

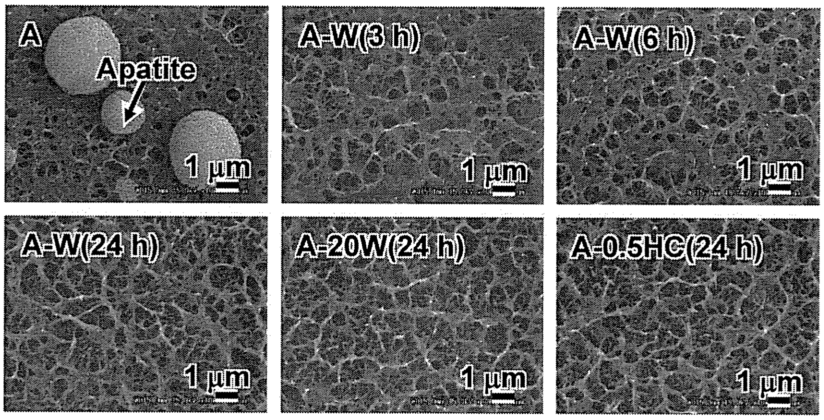

Fig. 7. FE–SEM images of surfaces on Ti plates subjected to NaOH, and water or HCl treatments, which were observed after soaking in SBF for 1 d.

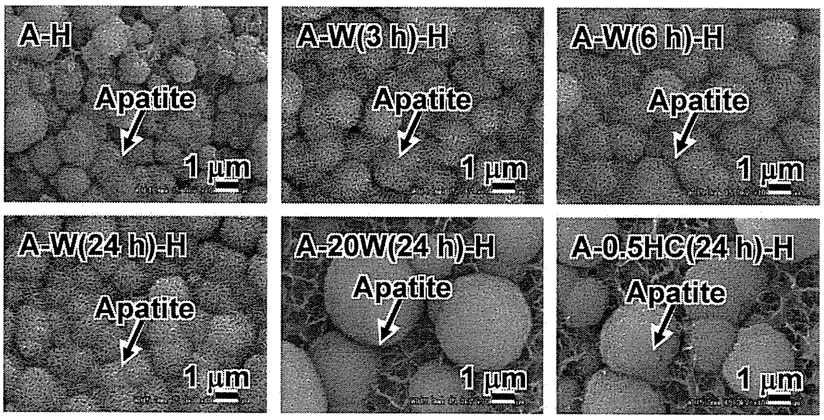

Fig. 8. FE–SEM images of surfaces on Ti plates subjected to NaOH, and water or HCl, then heat treatments, which were observed after soaking in SBF for 1 d.

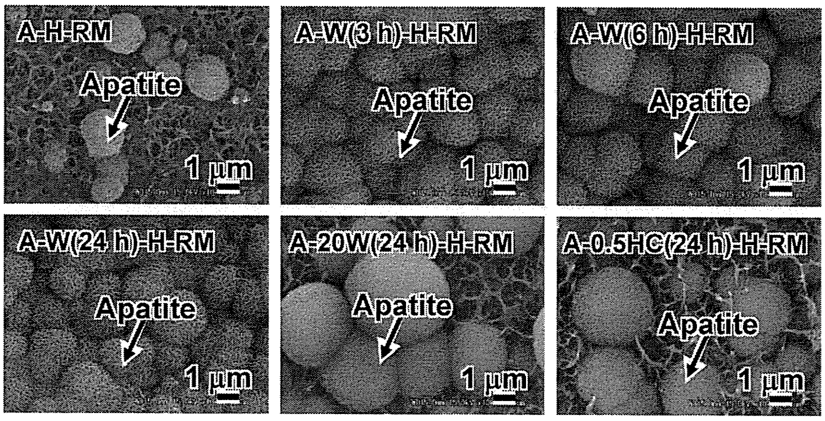

Fig. 9. FE–SEM images of surfaces on Ti plates subjected to NaOH, water or HCl, and heat treatments, which were kept in humid environment and soaked in SBF for 1 d.

3.3 Apatite-forming ability of the Ti plates

Figure 7 shows FE–SEM images of the surfaces of non-heated Ti plates taken after SBF-soaking for 1 d. Spherical particles newly observed on their surfaces were identified as an apatite by TF–XRD. The Ti plates subjected only to NaOH treatment and soaked in SBF acquired a partial coat of apatite within 1 d. This apatite-forming ability decreased with water or HCl treatment after the NaOH treatment.

Figure 8 shows FE–SEM images of the surfaces of heat-treated Ti plates taken after SBF-soaking for 1 d. It can be seen from the figure that all the heat-treated Ti plates acquired a full coat of apatite on their surfaces within 1 d, regardless of the kind of treatment before heating, although the surface layer treated with a large volume of water or HCl solution was covered with the apatite only 90% of its area.

Figure 9 shows FE–SEM images of the surfaces of heat-treated Ti plates, which were kept in humid environment at 80°C for 1 w and soaked in SBF for 1 d. It can be seen from Fig. 9 that the Ti plates subjected to water or HCl treatment after the NaOH treatment maintained their high apatite-forming abilities even after exposure to the humid environment for 1 w, whereas the Ti plate subjected to only NaOH treatment largely lost its apatite-forming ability in the same environment.

4. Discussion

It is apparent from the present experimental results described above that NaOH-treated Ti metal gives low apatite-forming ability (Fig. 7), as well as low scratch resistance (Fig. 6), before heat treatment, whereas it gives much higher apatite-forming ability (Fig. 8) and scratch resistance (Fig. 6) after the heat treatment, irrespective of the sodium content of its surface layer. Therefore, only the NaOH-treated Ti metal subjected to the subsequent heat treatment is practically important.

It is interesting to know from the experimental results described above that not only the apatite-forming ability of the heat-treated Ti metal does not decrease with decreasing sodium content in its surface layer, as far as the sodium ion is not completely removed (Figs. 1 and 8), but also its stability in humid environment is rather improved by the partial removal of the sodium ion in the surface layer (Fig. 9). These results might be interpreted as follows.

As revealed in the previous paper,[14] in the case of the NaOH- and heat-treated Ti metal, sodium titanate in the surface layer of the Ti metal releases the Na^+ ions to exchange with H_3O^+ ions in SBF to form a lot of Ti–OH groups on its surface, and to increase pH of the surrounding SBF. The Ti–OH groups are negatively charged in high pH environment and combine with positively charged Ca^{2+} ions. As the Ca^{2+} ions accumulate, the surface is positively charged and combines with phosphate ions to form apatite.

When the NaOH-treated Ti metal is treated with water, the sodium hydrogen titanate formed on the surfaces of the Ti metal by the NaOH treatment partially releases its Na^+ ions to exchange with the H_3O^+ ions in the water, and precipitates anatase as well as the sodium titanate by the subsequent heat treatments (Figs. 4 and 5). Thus formed anatase could have a lot of Ti–OH groups on its surface. As a result, they could induce apatite formation similar to the sodium titanate, as far as the sodium ions are released from the surface layer to give high pH environment. This might be the reason why the apatite-forming ability of the NaOH- and heat-treated Ti metal does not decrease with decreasing sodium content of the surface layer, as far as the sodium ion is not completely removed.

The sodium ions in the sodium titanate might also easily exchange with H_3O^+ ions in the moisture in the humid environment and are removed from its surface. As a result, the apatite-forming ability of the NaOH- and heat-treated Ti metal is liable to decrease in the humid environment after a long period. When the NaOH-treated Ti metal is treated with water or HCl solution and then subjected to the heat treatment, the top surface of the Ti metal is covered with the anatase. The anatase might be stable in the humid environment. As a result, the apatite-forming ability of the NaOH- and heat-treated Ti metal, in which sodium ions were partially or completely removed from its surface layer, is stable in humid environment.

It can be concluded from these results that the NaOH- and heat-treated Ti metal gives high apatite-forming ability as well as its high stability in humid environment, when the sodium ions in its surface layer is partially removed by the water treatment after the NaOH treatment.

5. Conclusion

The NaOH- and heat-treated Ti metal gives high apatite-forming ability, as well as its high stability in humid environment, when the Ti metal was treated with water after the first NaOH treatment, to partially remove the sodium ion in the surface layer and then subjected to heat treatment. The heat-treated Ti metal also shows high scratch resistance enough for handling by surgical devices.

References

1) T. Kokubo, F. Miyaji and H.-M. Kim, *J. Am. Ceram. Soc.*, 79, 1127–1129 (1996).
2) L. Jonášová, F. A. Müller, A. Helebrant, J. Strnad and P. Greil, *Biomaterials*, 23, 3095–3101 (2003).
3) T. Kokubo, H. Kushitani, S. Sakka, T. Kitsugi and T. Yamamuro, *J. Biomed. Mater. Res.*, 24, 721–734 (1990).
4) H. Takadama and T. Kokubo, *Biomaterials*, 27, 2907–2915 (2006).
5) Q. Chen, G. H. Du, S. Zhang and L. M. Peng, *Acta Crystallogr.*, B58, 587–593 (2002).
6) X. Sun and Y. Li, *Chem. Eur. J.*, 9, 2229–2238 (2003).
7) A. Nakahira, W. Kato, M. Tamai, T. Issiki and K. Nishio, *J. Mater. Sci.*, 39, 4239–4245 (2004).
8) Y. Mao, M. Kanungo, T. H-Benny and S. S. Wong, *J. Phys. Chem. B*, 110, 702–710 (2006).
9) Y. V. Kolen'ko, K. A. Kovnir, A. I. Gavrilov, A. V. Garshev, J. Frantti, O. I. Lebedev, B. R. Churagulov, G. V. Tendeloo and M. Yoshimura, *J. Phys. Chem. B*, 110, 4030–4038 (2006).
10) C. C. Tsai and H. Teng, *Chem. Mater.*, 18, 367–373 (2006).
11) D. V. Bavykin, J. M. Friendrich, A. A. Lapkin and F. C. Walsh, *Chem. Mater.*, 18, 1124–1129 (2006).
12) E. Morgado Jr, M. A. S de Abreu, O. R. C. Pravia, B. A. Marinkovic, P. M. Jardim, F. C. Rizzo and A. S. Araujo. *Solid State Sci.*, 8, 888–900 (2006).
13) H.-M. Kim, F. Miyaji, T. Kokubo and T. Nakamura, *J. Biomed. Mater. Res.*, 32, 409–417 (1996).
14) H. Takadama, H.-M. Kim, T. Kokubo and T. Nakamura, *J. Biomed. Mater. Res.*, 57, 441–448 (2001).

J Neurosurg Spine 13:500–508, 2010

Paraspinal-approach transforaminal lumbar interbody fusion for the treatment of lumbar foraminal stenosis

Clinical article

SHUNSUKE FUJIBAYASHI, M.D., PH.D., MASASHI NEO, M.D., PH.D., MITSURU TAKEMOTO, M.D., PH.D., MASATO OTA, M.D., AND TAKASHI NAKAMURA, M.D., PH.D.

Department of Orthopaedic Surgery, Graduate School of Medicine, Kyoto University, Sakyo-ku, Kyoto, Japan

Object. Foraminal stenosis is a common cause of lumbar radicular symptoms. Recognition of the dynamic pathology, as well as the static anatomical changes, is important to achieving successful surgical outcomes. Excessive facet and anulus removal leads to subsequent disc space narrowing and/or segmental instability, which can cause poor results after decompressive surgery. The objective of this study was to evaluate the efficacy of the paraspinal-approach transforaminal lumbar interbody fusion (TLIF) in the treatment of lumbar foraminal stenosis.

Methods. Twenty levels of lumbar foraminal stenosis in 16 patients were treated using an instrumented paraspinal-approach TLIF. There were 12 single-level and 4 two-level cases. Pathologies included foraminal stenosis at 13 levels and lateral disc herniation with disc space narrowing at 7.

Results. In all patients, preoperative radicular symptoms and mechanical low-back pain were resolved immediately after the operation and leg weakness improved gradually. The recovery rate using the Japanese Orthopaedic Association score was 89.1%. Bony union was achieved within 6 months after the operation in all cases. Postoperative MR imaging showed minimal changes in the paraspinal muscles in the single-level cases.

Conclusions. The paraspinal-approach TLIF is a minimally invasive, safe, and secure procedure for treating lumbar foraminal lesions. Direct visualization and decompression for the foraminal lesion, distraction of the collapsed disc space, and stabilization of the unstable segments can be achieved simultaneously through the paraspinal approach, which produces successful clinical and radiological results. *(DOI: 10.3171/2010.4.SPINE09691)*

KEY WORDS • foraminal stenosis • transforaminal lumbar interbody fusion • minimal invasiveness • paraspinal approach

FORAMINAL stenosis is a common cause of lumbar radicular symptoms. The incidence of lateral root entrapment as a cause of radicular pain is 8%–11%.[6,13,25] The lateral nerve root canal is a tubular-shaped region through which the nerve root passes from the thecal sac to the intervertebral foramen. Jenis and An[12] described the lumbar intervertebral foramen as a vertical interpedicular zone incorporating portions of the lateral recess and exit zone. The exiting nerve root and DRG are often located in the superior and anterior region of the foramen. The loss of intervertebral disc height secondary to desiccation and degeneration allows the superior articular process of the inferior vertebra to subluxate anteriorly and superiorly, diminishing the area of the foramen. The combination of disc space narrowing and overgrowth of structures anterior to the facet joint capsule may lead to anteroposterior stenosis. The exiting nerve root is compressed between the superior articular facet and the posterior vertebral body in a transverse direction.

An additional cause of foraminal stenosis is craniocaudal compression. Posterolateral osteophytes from the vertebral endplates protrude into the foramen along with a laterally bulging anulus fibrosis or herniated disc, compressing the nerve root against the superior pedicle. In

This article contains some figures that are displayed in color online but in black and white in the print edition.

Abbreviations used in this paper: DRG = dorsal root ganglion; JOA = Japanese Orthopaedic Association; PS = pedicle screw; TLIF = transforaminal lumbar interbody fusion.

TABLE 1: Summary of preoperative patient demographic data*

Case No.	Age (yrs), Sex	Main Pathology	Level	Sx	Preop JOA	Note
1	63, M	F-stenosis w/ lat disc herniation	L4–5	LP & LBP	11	
2	56, M	F-stenosis w/ lat disc herniation	L3–4	LP	14	
3	78, M	F-stenosis	L4–5	LP & LBP	14	
4†	53, F	F-stenosis	L3–4	LP & LBP	—	RA
5	58, F	F-stenosis w/ lat disc herniation	L5–S1	LP & LBP	17	
6	58, M	F-stenosis w/ lat disc herniation	L5–S1	LP	19	
7	63, M	F-stenosis	L5–S1	LP & LBP	21	previous op
8	70, F	F-stenosis	L4–5	LP	18	
9	62, M	L3–4 F-stenosis w/ lat disc herniation, L4–5 F-stenosis	L3–4, L4–5	LP & LBP	14	
10	58, M	L3–4 F-stenosis w/ lat disc herniation, L4–5 F-stenosis	L3–4, L4–5	LP	19	
11	59, F	F-stenosis	L3–4	LP & LBP	9	
12	75, M	F-stenosis	L3–4, L4–5	LP & LBP	18	
13	76, M	F-stenosis	L4–5	LP	22	
14	64, F	F-stenosis	L4–5	LP & LBP	17	PD
15	85, F	F-stenosis	L3–4, L4–5	LP & LW	8	previous op
16	60, M	F-stenosis	L4–5	LP & LBP	22	

* F-stenosis = foraminal stenosis; LBP = low-back pain; LP = leg pain; LW = leg weakness; PD = Parkinson disease; RA = rheumatoid arthritis.

† The patient with rheumatoid arthritis was excluded from the JOA score assessment.

addition to being aware of these static anatomical changes, it is important to consider the existence of dynamic stenosis. Fujiwara et al.[8] showed dynamic changes in the intervertebral foramen during flexion, extension, lateral bending, and axial rotation. The percentage change in cross-sectional foraminal area correlates with the amount of segmental motion.[11] Mechanical compression of the DRG and exiting nerve root may lead to low-back pain and radicular symptoms. Patients with foraminal stenosis may show variable degrees of leg and back pain, which may be exacerbated with lumbar extension to the painful side (the Kemp sign). Other common findings include focal motor weakness or diminished subjective sensation in a specific root distribution.

The initial treatment of lumbar radicular pain is conservative. Surgery is often needed for leg and back pain that is refractory to adequate conservative treatments. Surgical decompression may be accomplished through either a midline approach that includes interlaminar exposure, laminotomy or laminectomy, medial facetectomy, and medial foraminotomy or a muscle-splitting Wiltse or lateral approach to the foramen with foraminotomy.[30] In some instances, complete foraminal decompression may require a combined interlaminar and lateral approach. Advanced anular incompetence requires greater facet and anulus removal at the time of decompression and increases the possibility of postoperative segmental instability and asymmetrical disc space collapse. Secondary foraminal stenosis may lead to poor surgical results.[5]

Transforaminal lumbar interbody fusion is used increasingly as an alternative procedure for lumbar posterolateral fusion or posterior lumbar interbody fusion.[3,10,18,24] In the conventional midline approach, extensive muscle dissection and retraction leads to subsequent denervation and atrophy of the back muscles and may contribute to postoperative pain syndrome, such as fusion disease.[9,15,23,28] In general, one advantage of TLIF is that it is less invasive for the neural and posterior structures because of its unilateral approach. Numerous minimally invasive approaches have been developed recently to minimize approach-related morbidity.[7,14,17,20,22] Transforaminal lumbar interbody fusion through a paraspinal approach is one modality for minimally invasive surgery. We believe that TLIF is best for direct decompression of the stenotic intervertebral foramen with simultaneous stabilization. To our knowledge, our study is the first to evaluate the surgical outcomes of TLIF for the treatment of lumbar foraminal stenosis. We describe the clinical and radiological results and the surgical technique of this paraspinal-approach TLIF for lumbar foraminal stenosis.

Methods

Sixteen consecutive patients (10 men and 6 women) with lumbar foraminal stenosis were treated surgically using a paraspinal-approach TLIF between November 2005 and August 2008. Their mean age at surgery was 64.9 years (range 53–85 years). Twenty levels were treated, including 12 single-level and 4 two-level cases. The numbers of fused segments were 7 levels at L3–4, 10 levels at L4–5, and 3 levels at L5–S1. The follow-up period was at least 12 months.

Preoperatively, 10 patients had both leg pain and low-back pain, 5 had leg pain without low-back pain, and 1 had leg pain and leg weakness. In all 16 cases, these symptoms were refractory to adequate conservative treatment (Table 1). The average preoperative JOA score was 16.2 (Table 2). One patient with rheumatoid arthritis who had previously undergone multiple joint surgeries was excluded from JOA score assessment. Diagnosis was confirmed by diagnostic selective nerve root block in all but the one patient with leg weakness. Magnetic resonance imaging and multidetector-row CT were used to assess the static anatomical changes in the foramen, and lateral dynamic radiographs were used to assess the dynamic situation. Concordance between the demonstrated areas of stenosis in MR imaging and CT and radicular symptoms was evaluated carefully.

The inclusion criteria in the radiological examinations were the existence of foraminal stenosis with disc degeneration at the affected levels, with or without segmental instability, and with or without lateral disc herniation. The affected disc degeneration was Grade 3, which equated to a finding of signal hypointensity on T2-weighted MR images with disc space narrowing in all patients according to the classification of Schneiderman et al.[21] The vacuum phenomenon was recognized in 17 affected discs (85%). Preoperative dynamic lateral radiographs showed marked instability at 13 levels (65%), which included 4 levels of spondylolisthesis and 9 levels of retrolisthesis. To evaluate the direct effect of TLIF in the treatment of foraminal lesions, patients with combined central canal stenosis (double crush syndrome) or lateral recess stenosis were excluded. In addition, patients were excluded if they had lateral disc herniation without significant disc space narrowing, which could be treated by removal of the herniated disc material via interlaminar or extralaminar approaches depending on the location of the lesion.

Radiological Assessments

To assess bony union, lateral dynamic radiographs were obtained at 6 months and at the final follow-up examination. More than 2° of motion on flexion-extension was considered to indicate nonunion. In addition, radiolucencies around the PSs and titanium cage were defined as nonunion. Computed tomography assessment of the coronal and sagittal reconstruction views was performed 6 months after surgery. Bone union was defined as solid when there was osseous continuity around the cage on both the coronal and sagittal reconstructed CT images. Nonunion was defined as the presence of a visible gap between the vertebral endplate and cage or radiolucency around the PSs on CT. Radiologically successful fusion was diagnosed when the assessments of radiological parameters mentioned above were complete. Cage migration of 3 mm or more into the vertebral endplate was defined as significant cage subsidence.

The disc height and foraminal height were measured using lateral radiographs obtained in a neutral position. The disc height was calculated as the average of the anterior disc height (A in Fig. 1) and the posterior disc height (B in Fig. 1). The foraminal height was measured as the distance between the pedicles. Preoperative and postoperative values were analyzed statistically using the paired

TABLE 2: Summary of JOA score classifications for low-back pain*

Parameter	JOA Score
subjective Sx	9
low-back pain	
none	3
occasional mild pain	2
frequent mild or occasional severe pain	1
frequent or continuous severe pain	0
leg pain &/or tingling	
none	3
occasional slight Sx	2
frequent slight or occasional severe Sx	1
frequent or continuous severe Sx	0
gait	
normal	3
able to walk >500 m, although it causes pain, tingling, &/or muscle weakness	2
unable to walk >500 m due to leg pain, tingling, &/or muscle weakness	1
unable to walk >100 m due to leg pain, tingling, &/or muscle weakness	0
clinical signs	6
straight leg-raising test (including tight hamstrings)	
normal	2
30–70°	1
<30°	0
sensory disturbance	
none	2
slight disturbance (not subjective)	1
marked disturbance	0
motor disturbance	
normal (Grade 5/5)	2
slight weakness (Grade 4/5)	1
marked weakness (Garde 0–3/5)	0
restriction of ADL†	14
ADL (restriction)	
turning over while lying down	
standing	
washing	
leaning forward	
sitting (~1 hr)	
lifting/holding heavy objects	
walking	
urinary bladder function	−6
normal	0
mild dysuria	−3
severe dysuria (incontinence, urinary retention)	−6

* ADL = activities of daily living.

† For each ADL category, severe restriction was accorded a score of 0; moderate restriction, a score of 1; and no restriction, a score of 2.

t-test and a p value < 0.05 was considered statistically significant.

To evaluate paravertebral muscle injury, axial T2-weighted MR images of the fused segment obtained at 6 months after surgery were compared with the preoperative images with respect to the original grading system on both sides. Grade 0 indicated no signal change within the multifidus muscle; Grade 1, signal change in less than 50% of the cross-sectional area of the multifidus muscle, Grade 2, signal change in more than 50% of the area; and Grade 3, signal change in more than 50% of the area with atrophy (Fig. 2).

Surgical Procedures

In cases of L4–5 foraminal stenosis, a midline skin incision of approximately 7 cm in length is performed from L-3 to L-5. The thoracolumbar fascia is incised longitudinally close to the supraspinous ligament. The interfascial plane between the thoracolumbar fascia and superficial fascia of the multifidus muscle is dissected bluntly. The superficial fascia of multifidus muscle is incised in line with the fiber about 2–3 cm lateral to the midline. The lateral aspect of the facet joint is exposed through blunt dissection between the multifidus muscle and the longissimus muscle using a fingertip. The operation field is maintained using Gelpi retractors, which must be relaxed intermittently to reduce direct muscle injury. After bilateral placement of the PSs under the guidance of anteroposterior and lateral fluoroscopy, the neural foramen is exposed by excision of the inferior articular process of L-4 and the superior articular process of L-5 using a chisel and Kerrison rongeur to harvest local bone under surgical microscopy (Fig. 3 left). The disc is fenestrated at the safety triangle zone between the exiting nerve root and the traversing nerve root. The disc space is opened sequentially using disc distractors, and the distracted space is maintained using a PS self-distractor. After meticulous endplate preparation, the bone chips are packed in the anterior space, and an adequate-sized titanium cage (Boomerang II cage, Medtronic Sofamor Danek) is placed centrally in the intervertebral space along with either a custom-made porous hydroxyapatite spacer (Apaceram, Pentax Co.) or the local bone chips. Additional local bone chips are packed posterior to the cage. Contralateral facet fusion with local bone graft is performed to achieve 360° fusion after adequate removal of articular cartilage (Fig. 3 right). In cases of insufficient local bone volume, additional autogenous bone is harvested from the ilium.

Results

In all 16 patients, the preoperative radicular symptoms and mechanical low-back pain resolved immediately after the operation; leg weakness improved gradually and had resolved completely by 3 months after the operation. No surgery-related neurological deficit or wound breakdown was observed in any patient. The patients were allowed to ambulate while wearing a hard brace beginning on the 1st day after surgery. The average postoperative JOA score was 27.4 (range 23–29). The average recovery rate of the JOA score was 89.1% (range 58.3–100%). (The recovery rate was calculated as a percentage as follows: [postoperative score – preoperative score]/[29 (full score) – preoperative score] × 100). Eight patients recovered to the full score; these patients reported no lumbar spine–related complaints postoperatively. The mean operating time was 187.5 minutes (range 130–289 minutes), and the mean estimated intraoperative blood loss was 274 ml (range 30–720 ml). No patient required transfusion. The intraoperative findings showed that the main pathologies of the foraminal region for nerve root compression included 13 patients with foraminal stenosis and 7 with foraminal stenosis with lateral disc herniation. In 11 patients (68.7%) only local bone—with or without a hydroxyapatite spacer—was used for grafting, and in the remaining 5 the addition of iliac crest bone was required. There was only 1 surgery-related complication, a PS misplacement that required a revision operation (Case 7, Table 3). No patient experienced symptom aggravation. The mean follow-up period was 23.1 months (range 12–45 months).

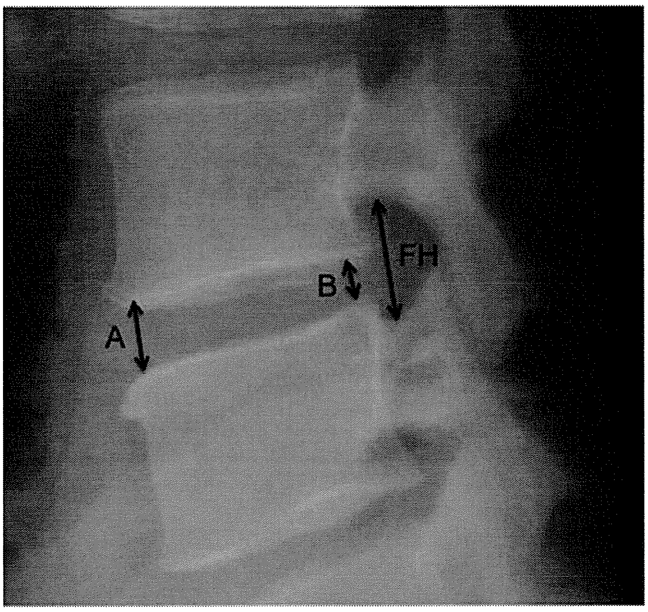

Fig. 1. Disc height and foraminal height (FH) were measured using lateral radiographs obtained in the neutral position. Disc height was calculated as the average of the anterior disc height (A) and posterior disc height (B). Foraminal height was measured as the distance between the pedicles.

Radiological Results

Radiological evidence of solid bony union was observed in all patients by 6 months after the operation. No patient exhibited significant cage subsidence. One case of symptomatic disc herniation at the adjacent segment was recognized at 40 months after the initial surgery and was successfully treated conservatively. The mean disc height increased from 5.2 mm (range 1.0–10.1 mm) before the operation to 8.8 mm (range 6.6–11.5 mm) after the operation, which was a statistically significant difference (p < 0.001). The foraminal height increased from 10.4 mm (range 4.9–11.9 mm) before the operation to 14.5 mm (range 11.6–18.3 mm) after the operation, which was also a statistically significant difference (p < 0.001).

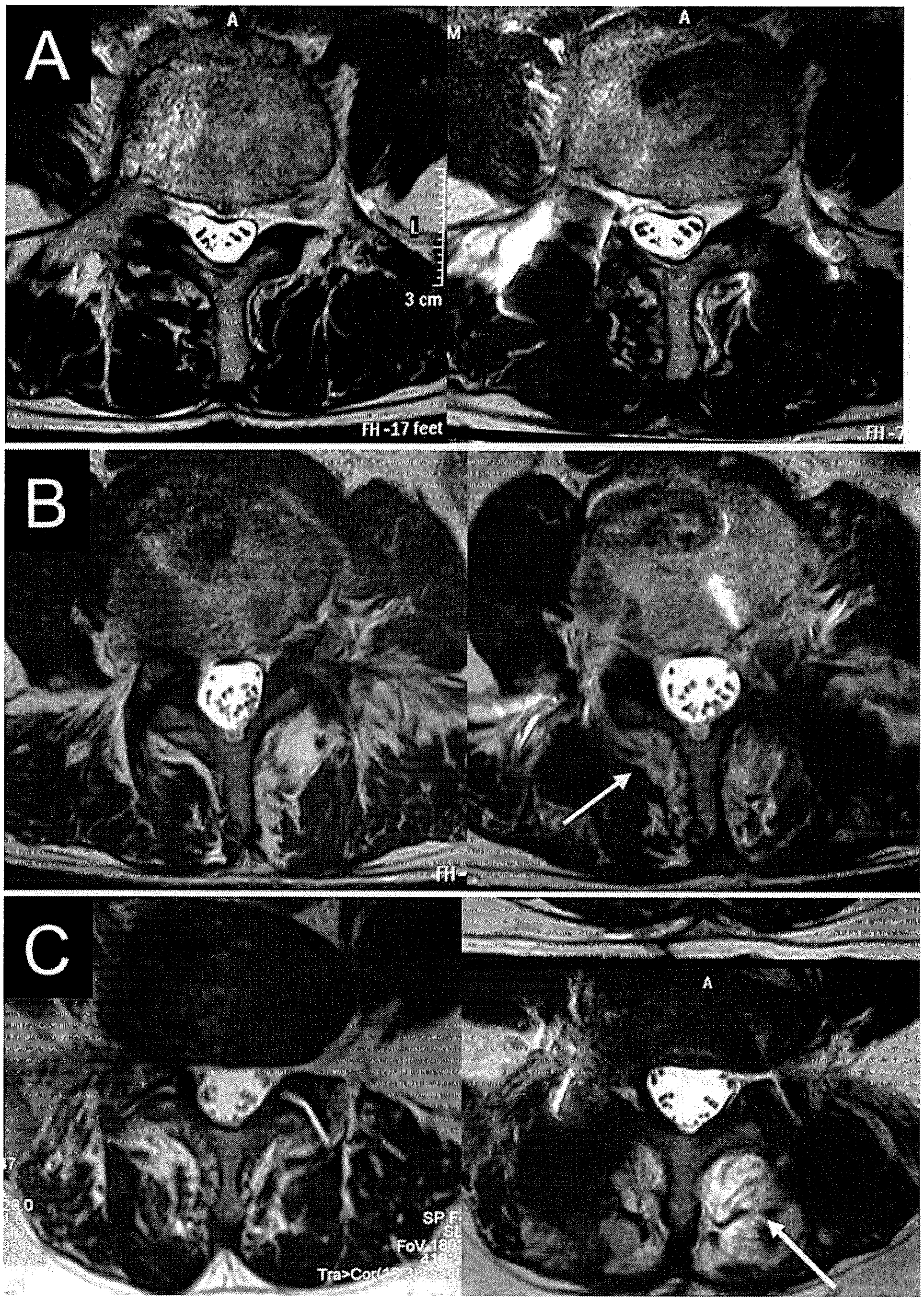

Fig. 2. Magnetic resonance imaging grades of paravertebral muscle injury. Preoperative images are shown on the **left** and postoperative images on the **right**. **A:** Typical case of Grade 0 with no signal change in the multifidus muscle. **B:** Typical case of Grade 1 with signal change in less than 50% of the cross-sectional area of the multifidus. The *arrow* indicates muscle degenerative changes in the deep layer of the muscle. **C:** Typical case of Grade 2 with signal change in more than 50% of the multifidus area. The *arrow* indicates muscle degenerative changes in the multifidus muscle.

Thirty-four areas of 17 spinal levels in 14 patients could be assessed by MR imaging at 6 months after the operation. The signal intensity change was Grade 0 in 8 areas (23.5%), Grade 1 in 22 areas (64.7%), Grade 2 in 4 areas (11.8%), and Grade 3 in no areas. The preoperative and postoperative clinical and radiological results are summarized in Table 3.

Illustrative Case

Foraminal Stenosis With Lateral Disc Herniation (Case 6)

This 58-year-old man complained of mechanical low-back pain and intractable right leg pain and dysesthesia on the right L-5 sensory dermatome. A radiograph showed severe collapse of the L5–S1 disc space with in-

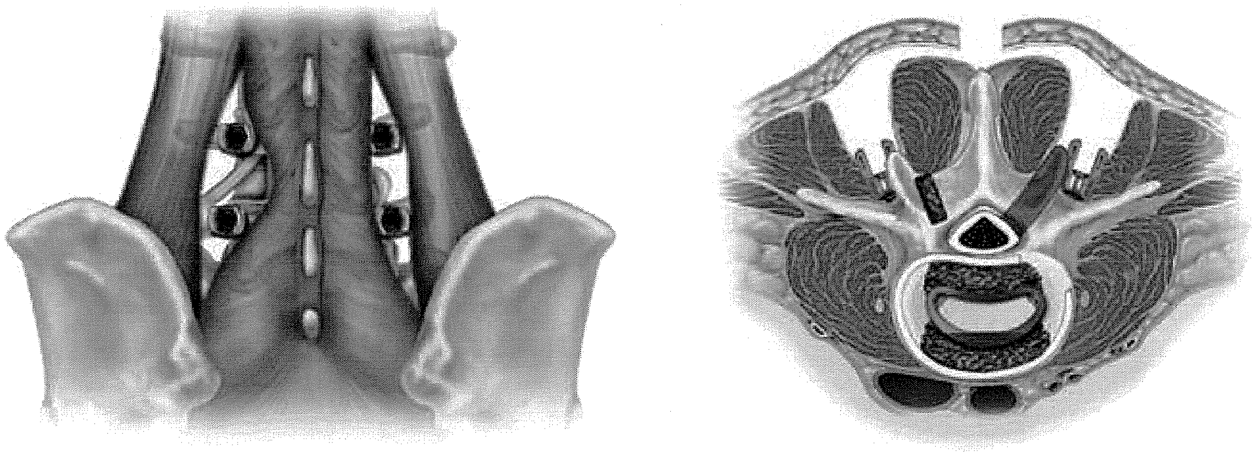

Fig. 3. Artist's illustration of the paraspinal-approach TLIF. **Left:** Bilateral paraspinal approach, placement of the PSs, and exposure of the neural foramen after excision of the unilateral facet joint. **Right:** Interbody placement of the titanium cage combined with porous hydroxyapatite spacer and grafting of autologous local bone chips around the cage and contralateral facet joint.

stability. An MR imaging study showed bilateral foraminal stenosis combined with a right-side lateral herniated disc at the L5–S1 level (Fig. 4A and B). A preoperative L-5 nerve root injection effectively controlled his leg pain for a few days. The operative procedure was paraspinal TLIF at L5–S1 (Fig. 4C and D). Pedicle screw placement in the inversion angle was achieved through a paraspinal approach. The operating time was 150 minutes, and the estimated intraoperative blood loss was 230 ml. At 6 months after the operation, CT showed successful bony union (Fig. 4E), MR imaging showed a Grade 1 change of the paravertebral muscle on both sides (Fig. 4F), and the patient was free of complaints with a full JOA score of 29 points.

Discussion

Sixteen patients with lumbar foraminal stenosis were treated successfully using a paraspinal-approach TLIF. Marked improvements in clinical outcomes and low incidence of paraspinal muscle injury represent the potential benefits of minimally invasive spinal fusion technique.

TABLE 3: Summary of clinical and radiological outcomes*

Case No.	Op Time (min)	Blood Loss (ml)	Bone Graft	Postop JOA	Recovery Rate (%)	Bony Union	MRI Grading† (rt/lt)	Complication	ASD	FU Period (mos)
1	168	139	local	29	100	union	0/0	none	HNP	45
2	203	144	local	29	100	union	1/1	none	none	43
3	196	465	local	27	86.6	union	1/0	none	none	30
4‡	136	300	iliac	—	—	union	1/1	none	none	27
5	211	227	local	24	58.3	union	—	none	none	27
6	150	230	local	29	100	union	0/1	none	none	25
7	192	205	HA + local	29	100	union	1/1	PS misplacement	none	24
8	200	440	HA + local	29	100	union	1/1	none	none	23
9	289	720	local	23	60	union	—	none	none	19
10	206	206	HA + local	29	100	union	L3–4 1/1, L4–5 1/1	none	none	18
11	147	120	iliac	23	70	union	1/1	none	none	17
12	230	328	iliac	29	100	union	L3–4 1/0, L4–5 2/2	none	none	16
13	185	200	HA + local	29	100	union	1/1	none	none	16
14	140	30	iliac	28	91.6	union	0/1	none	none	15
15	218	530	iliac	26	85.7	union	L3–4 1/1, L4–5 2/2	none	none	12
16	130	100	HA + local	28	85.7	union	0/0	none	none	12

* ASD = adjacent-segment disease; FU = follow-up; HA = hydroxyapatite spacer; HNP = herniated nucleus pulposus.

† Grades on MR imaging defined as follows: Grade 0, no signal change; Grade 1, signal change in less than 50% of area; Grade 2, signal change in more than 50% of area; Grade 3, signal change in more than 50% of area with atrophy.

‡ This patient had rheumatoid arthritis and was excluded from the JOA score and recovery rate assessment.

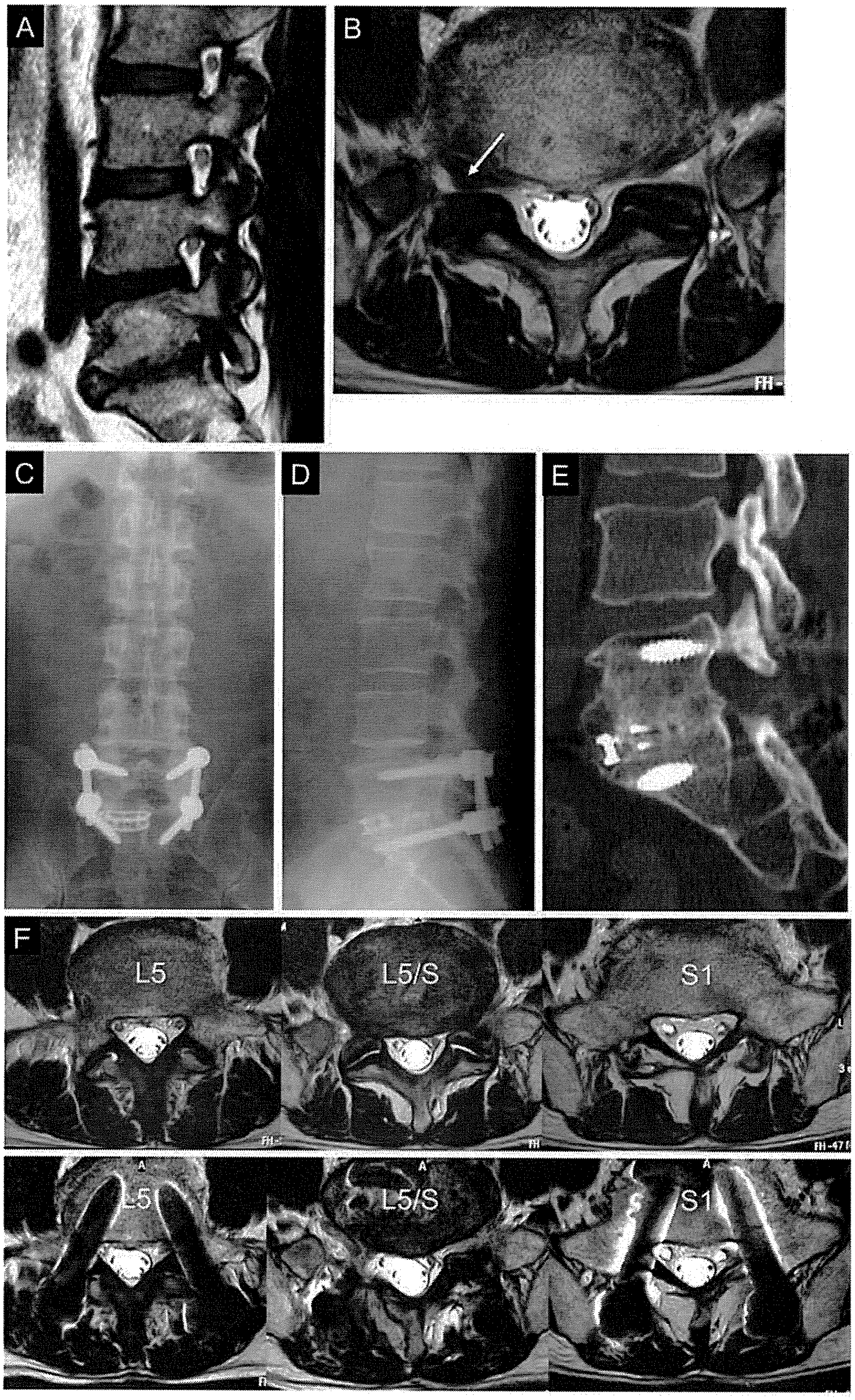

FIG. 4. Case 6. Preoperative and postoperative radiological studies obtained in a 58-year-old man with foraminal stenosis combined with lateral disc herniation at L5–S1. **A:** Parasagittal MR image demonstrating foraminal stenosis with a Modic change of the vertebral endplate. **B:** Axial MR image demonstrating foraminal stenosis with lateral disc herniation *(arrow)* on the right side at the L5–S1 level. **C and D:** Anteroposterior and lateral radiographs demonstrating good positioning of the interbody cage and PSs. **E:** Sagittal reconstruction CT image demonstrating solid bony union into and around the cage 6 months after surgery. **F:** Axial MR images demonstrating minimal changes in the paraspinal muscles before surgery **(upper)** and 6 months after surgery **(lower)**.

Unrecognized or recurrent foraminal stenosis may be associated with failed back surgery syndrome. In a review of failed back surgery syndrome, Burton et al.[4] attributed the condition to the lack of recognition or inadequate treatment of nonspecific lateral canal stenosis and considered it to be the cause of pain in nearly 60% of patients with continued postoperative symptoms. Adequate preoperative diagnosis of foraminal lesions is important to achieving successful surgical results. Parasagittal and coronal MR images and axial and parasagittal CT images are mainstays for evaluating and quantifying the degree of foraminal stenosis. However, the false-positive and false-negative rates are high.[1,2] Concordance of imaging studies, selective nerve root block, and clinical symptoms are the keys to making a correct diagnosis. In the current study, all but 1 patient, who was paralytic, experienced immediate pain relief after selective nerve root block, which reflected the correct diagnosis and subsequent successful surgical results.

The disadvantages of decompressive surgery via interlaminar or/and extralaminar access include incomplete decompression and blind maneuvers around the DRG. Because the transforaminal ligaments are attached to the superior articular facet, the superior articular facet must be excised to expose the neural foramen completely.[16] The DRG is sensitive to mechanical pressure, and excessive manipulation of the DRG leads to worsening postoperative symptoms, such as persistent dysesthesia and complex regional pain syndrome Type I.[19] In addition, excessive facet and anulus removal at the time of decompression increases the possibility of postoperative segmental instability and asymmetrical disc space collapse and leads to poor surgical results.[5]

The insertion of an interbody implant allows the distraction of the disc space and subsequent enlargement of the intervertebral foramen. Posterior lumbar interbody fusion is considered an indirect foraminal enlargement procedure. In this procedure, the posterior midline structures such as the paravertebral muscle, spinous process, and laminae must be excised to place the intervertebral implants, and this procedure may cause postoperative denervation of posterior structures.[9,15,23,28] In addition, medial retraction of the traversing nerve root and dural tube is necessary to place the intervertebral implants, and this may cause neural tissue damage and epidural scar formation.

A paraspinal-approach TLIF is a safe and minimally invasive procedure that can be used to decompress and stabilize lesions in the stenotic foramen. The paraspinal approach to the lumbar spine was introduced by Wiltse.[26,29,30] The lateral parts of the facet joint can be exposed easily by blunt dissection through the cleavage plane between the multifidus and the longissimus parts of the sacrospinalis muscle at the cranial to L4–5 level. In cases involving L5–S1 exposure, detachment of the multifidus muscle from the longissimus parts of the sacrospinalis allows good visualization because the multifidus muscle courses obliquely and dorsolaterally to attach to the longissimus parts of the sacrospinalis and the ilium.[27] The paraspinal approach can allow good visualization and maintain a wide field for the surgical maneuver. Direct visualization of compressive pathologies by complete removal of the facet joint and surrounding soft tissue, and stabilization of unstable spinal segments to resolve the dynamic lesion at the same time, are safe and secure procedures. The TLIF has the following advantages: 1) It requires a single midline skin incision. 2) It is minimally invasive to the posterior midline structure. 3) It allows medially oriented PS placement. 4) It allows direct visualization and decompression of the intraforaminal lesion. 5) It requires an easily applied distraction and compression maneuver through manipulation of the collapsed disc space and the placed PSs. 6) Disc space enlargement can be achieved by the placement of an interbody spacer. 7) It permits a combination of contralateral facet fusion to achieve circumferential fusion.

Postoperative MR imaging confirmed the minimal invasiveness on the posterior structures. In the current series, in patients with a single-level fusion, the muscle injury grade was limited to 0–1. In contrast, 2 of the patients with a double-level fusion exhibited Grade 2 injury at the caudal level, although the radiological results were not related to the clinical results. A possible disadvantage of the paraspinal approach is direct injury to the medial, muscular, or lateral branch of the posterior ramus, which is related to denervation of the multifidus muscle. The surgeon should be aware that multilevel fusion through the paraspinal approach has potential to cause direct nerve injury and subsequent muscle denervation.

Conclusions

Sixteen patients with lumbar foraminal stenosis were treated successfully using a paraspinal-approach TLIF. We conclude that the paraspinal-approach TLIF is a minimally invasive, safe, and secure procedure to treat lumbar foraminal lesions. Direct visualization and decompression of the foraminal lesion, distraction of the disc space by the placement of an interbody spacer, and stabilization of unstable segments can be achieved simultaneously through the paraspinal approach, which produces successful clinical and radiological outcomes.

Disclosure

The authors report that no funds were received in support of this study and no benefits in any form have been or will be received from a commercial party related directly or indirectly to the subject of this manuscript.

Author contributions to the study and manuscript preparation include the following. Conception and design: Fujibayashi. Acquisition of data: Fujibayashi. Analysis and interpretation of data: Fujibayashi. Drafting the article: Fujibayashi. Critically revising the article: Fujibayashi. Reviewed final version of the manuscript and approved it for submission: all authors. Statistical analysis: Fujibayashi. Study supervision: Neo, Nakamura.

References

1. Aota Y, Niwa T, Yoshikawa K, Fujiwara A, Asada T, Saito T: Magnetic resonance imaging and magnetic resonance myelography in the presurgical diagnosis of lumbar foraminal stenosis. **Spine 32:**896–903, 2007
2. Attias N, Hayman A, Hipp JA, Noble P, Esses SI: Assessment

of magnetic resonance imaging in the diagnosis of lumbar spine foraminal stenosis—a surgeon's perspective. **J Spinal Disord Tech 19:**249–256, 2006
3. Blume HG: Unilateral posterior lumbar interbody fusion: simplified dowel technique. **Clin Orthop Relat Res 193:**75–84, 1985
4. Burton CV, Kirkaldy-Willis WH, Yong-Hing K, Heithoff KB: Causes of failure of surgery on the lumbar spine. **Clin Orthop Relat Res 157:**191–199, 1981
5. Chang SB, Lee SH, Ahn Y, Kim JM: Risk factor for unsatisfactory outcome after lumbar foraminal and far lateral microdecompression. **Spine 31:**1163–1167, 2006
6. Cinotti G, De Santis P, Nofroni I, Postacchini F: Stenosis of lumbar intervertebral foramen: anatomic study on predisposing factors. **Spine 27:**223–229, 2002
7. Dhall SS, Wang MY, Mummaneni PV: Clinical and radiographic comparison of mini-open transforaminal lumbar interbody fusion with open transforaminal lumbar interbody fusion in 42 patients with long-term follow-up. **J Neurosurg Spine 9:**560–565, 2008
8. Fujiwara A, An HS, Lim TH, Haughton VM: Morphologic changes in the lumbar intervertebral foramen due to flexion-extension, lateral bending, and axial rotation: an in vitro anatomic and biomechanical study. **Spine 26:**876–882, 2001
9. Gejo R, Matsui H, Kawaguchi Y, Ishihara H, Tsuji H: Serial changes in trunk muscle performance after posterior lumbar surgery. **Spine 24:**1023–1028, 1999
10. Harms JG, Jeszenszky D: The unilateral transforaminal approach for posterior lumbar interbody fusion. **Orthop Traumatol 6:**88–99, 1998
11. Inufusa A, An HS, Lim TH, Hasegawa T, Haughton VM, Nowicki BH: Anatomic changes of the spinal canal and intervertebral foramen associated with flexion-extension movement. **Spine 21:**2412–2420, 1996
12. Jenis LG, An HS: Spine update. Lumbar foraminal stenosis. **Spine 25:**389–394, 2000
13. Kunogi J, Hasue M: Diagnosis and operative treatment of intraforaminal and extraforaminal nerve root compression. **Spine 16:**1312–1320, 1991
14. Lee DY, Jung TG, Lee SH: Single-level instrumented mini-open transforaminal lumbar interbody fusion in elderly patients. **J Neurosurg Spine 9:**137–144, 2008
15. Macnab I, Cuthbert H, Godfrey CM: The incidence of denervation of the sacrospinales muscles following spinal surgery. **Spine 2:**294–298, 1977
16. Min JH, Kang SH, Lee JB, Cho TH, Suh JG: Anatomic analysis of the transforaminal ligament in the lumbar intervertebral foramen. **Neurosurgery 57 (1 Suppl):**37–41, 2005
17. Mummaneni PV, Rodts GE Jr: The mini-open transforaminal lumbar interbody fusion. **Neurosurgery 57 (4 Suppl):**256–261, 2005
18. Potter BK, Freedman BA, Verwiebe EG, Hall JM, Polly DW Jr, Kuklo TR: Transforaminal lumbar interbody fusion: clinical and radiographic results and complications in 100 consecutive patients. **J Spinal Disord Tech 18:**337–346, 2005
19. Raja SN, Grabow TS: Complex regional pain syndrome I (reflex sympathetic dystrophy). **Anesthesiology 96:**1254–1260, 2002
20. Scheufler KM, Dohmen H, Vougioukas VI: Percutaneous transforaminal lumbar interbody fusion for the treatment of degenerative lumbar instability. **Neurosurgery 60 (4 Suppl 2):**203–213, 2007
21. Schneiderman G, Flannigan B, Kingston S, Thomas J, Dillin WH, Watkins RG: Magnetic resonance imaging in the diagnosis of disc degeneration: correlation with discography. **Spine 12:**276–281, 1987
22. Schwender JD, Holly LT, Rouben DP, Foley KT: Minimally invasive transforaminal lumbar interbody fusion (TLIF): technical feasibility and initial results. **J Spinal Disord Tech 18 (Suppl):**S1–S6, 2005
23. Sihvonen T, Herno A, Paljärvi L, Airaksinen O, Partanen J, Tapaninaho A: Local denervation atrophy of paraspinal muscles in postoperative failed back syndrome. **Spine 18:**575–581, 1993
24. Taneichi H, Suda K, Kajino T, Matsumura A, Moridaira H, Kaneda K: Unilateral transforaminal lumbar interbody fusion and bilateral anterior-column fixation with two Brantigan I/F cages per level: clinical outcomes during a minimum 2-year follow-up period. **J Neurosurg Spine 4:**198–205, 2006
25. Vanderlinden RG: Subarticular entrapment of the dorsal root ganglion as a cause of sciatic pain. **Spine 9:**19–22, 1984
26. Vialle R, Wicart P, Drain O, Dubousset J, Court C: The Wiltse paraspinal approach to the lumbar spine revisited: an anatomic study. **Clin Orthop Relat Res 445:**175–180, 2006
27. Weaver EN Jr: Lateral intramuscular planar approach to the lumbar spine and sacrum. Technical note. **J Neurosurg Spine 7:**270–273, 2007
28. Weber BR, Grob D, Dvorák J, Müntener M: Posterior surgical approach to the lumbar spine and its effect on the multifidus muscle. **Spine 22:**1765–1772, 1997
29. Wiltse LL: The paraspinal sacrospinalis-splitting approach to the lumbar spine. **Clin Orthop Relat Res 91:**48–57, 1973
30. Wiltse LL, Bateman JG, Hutchinson RH, Nelson WE: The paraspinal sacrospinalis-splitting approach to the lumbar spine. **J Bone Joint Surg Am 50:**919–926, 1968

Manuscript submitted August 24, 2009.

Accepted April 6, 2010.

Address correspondence to: Shunsuke Fujibayashi, M.D., Ph.D., Department of Orthopaedic Surgery, Graduate School of Medicine, Kyoto University, 54 Shogoin Kawahara-cho, Sakyo-ku, Kyoto 606-8507, Japan. email: shfuji@kuhp.kyoto-u.ac.jp.

SPINE Volume 35, Number 18, pp E895–E903
©2010, Lippincott Williams & Wilkins

Computer-Assisted Spinal Osteotomy

A Technical Note and Report of Four Cases

Shunsuke Fujibayashi, MD, PhD,* Masashi Neo, MD, PhD,* Mitsuru Takemoto, MD, PhD,*
Masato Ota, MD,* Tomitaka Nakayama, MD, PhD,* Junya Toguchida, MD, PhD,†
and Takashi Nakamura, MD, PhD*

Study Design. A report of 4 cases of spinal osteotomy performed under the guidance of a computer-assisted navigation system and a technical note about the use of the navigation system for spinal osteotomy.

Objective. To document the surgical technique and usefulness of computer-assisted surgery for spinal osteotomy.

Summary of Background Data. A computer-assisted navigation system provides accurate 3-dimensional (3D) real-time surgical information during the operation. Although there are many reports on the accuracy and usefulness of a navigation system for pedicle screw placement, there are few reports on the application for spinal osteotomy.

Methods. We report on 4 complex cases including 3 solitary malignant spinal tumors and 1 spinal kyphotic deformity of ankylosing spondylitis, which were treated surgically using a computer-assisted spinal osteotomy. The surgical technique and postoperative clinical and radiologic results are presented.

Results. 3D spinal osteotomy under the guidance of a computer-assisted navigation system was performed successfully in 4 patients. All malignant tumors were resected *en bloc*, and the spinal deformity was corrected precisely according to the preoperative plan. Pathologic analysis confirmed the *en bloc* resection without tumor exposure in the 3 patients with a spinal tumor.

Conclusion. The use of a computer-assisted navigation system will help ensure the safety and efficacy of a complex 3D spinal osteotomy.

Key words: computer-assisted navigation system, spinal osteotomy, spinal tumor, ankylosing spondylitis. **Spine 2010;35:E895–E903**

Computer-assisted surgery was developed to decrease the intraoperative radiologic exposure to patients and physicians, to increase the accuracy of surgery, and to allow the surgeon to perform spine surgery safely. Many recent reports show that a computer-assisted navigation system increases the accuracy of pedicle screw placement.[1,2] The usefulness of such navigation systems in the excision of ossification of the posterior longitudinal ligament, ossification of the ligamentum flavum, and some kinds of spinal tumors have also been reported.[3–9] Use of a navigation system also increases the accuracy of the placement of implants in joint arthroplastic surgery,[10] deformed long bone osteotomy, and high tibial osteotomy. Such navigation systems provide 3-dimensional (3D) information, which allows the surgeon to correct the deformity more precisely.[11–13] A navigation system increases the surgical accuracy by providing precise real-time information to the surgeon about the intraoperative orientation and localization. Although precise 3D information is required during a spinal osteotomy to decrease the neurovascular complications, there are few reports on the application of a navigation system in this type of operation.[14,15]

In the current study, we describe the successful operations using 3D spinal osteotomy on 4 complex patients, including 3 patients with a malignant tumor and 1 with spinal deformity, under the guidance of a computer-assisted navigation system. The aim of this article is to describe the surgical technique and the usefulness of computer-assisted surgery for spinal osteotomy.

■ Materials and Methods

Three patients with malignant spinal tumors, which included metastatic hepatocellular carcinoma, chondrosarcoma, and fibrosarcoma, and 1 patient with a fixed kyphotic deformity as a result of ankylosing spondylitis were treated surgically using a spinal osteotomy. The level of osteotomy was the thoracic spine in 2 patients and the lumbar spine in 2 patients. The patients' preoperative demographic data are summarized in Table 1.

Computer-Assisted Technique

The navigation system used in this study was the StealthStation TRIA (Medtronic Sofamor Danek, Memphis, TN). The navigation system comprised a computer workstation, reference frame with passive markers, standard probe, and electro-optical camera connected to the computer workstation, which served as a position sensor. The basic data used for navigation included the preoperative computed tomography (CT) imaging data (slice thickness, 1 mm). The data were transferred and recorded on the system computer and reconstructed into 3D images. The registration procedures of the point merging and surface merging produced 3D spinal images on the monitor that were identical to the actual appearance of the spine in the operative field.

After exposing the posterior element, the reference frame of the navigation system was mounted on the exposed spinous process. In cases involving an unfamiliar operative position,

---

From the *Department of Orthopaedic Surgery, Graduate School of Medicine, Kyoto University, Kyoto, Japan; and †Department of Tissue Regeneration, Institute for Frontier Medical Sciences, Kyoto University, Kyoto, Japan.

Acknowledgment date: July 10, 2009. First revision date: December 9, 2009. Second revision date: February 7, 2010. Acceptance date: February 8, 2010.

The manuscript submitted does not contain information about medical device(s)/drug(s).

No funds were received in support of this work. No benefits in any form have been or will be received from a commercial party related directly or indirectly to the subject of this manuscript.

Address correspondence and reprint requests to Shunsuke Fujibayashi, MD, PhD, Department of Orthopaedic Surgery, Graduate School of Medicine, Kyoto University, 54 Shogoin Kawahara-cho, Sakyo-ku, Kyoto 606-8507, Japan; E-mail: shfuji@kuhp.kyoto-u.ac.jp